

The C-Band All-Sky Survey (C-BASS): Total intensity point source detection over the northern sky

R.D.P. Grumitt,^{1*} Angela C. Taylor,¹ Luke Jew,¹ Michael E. Jones,¹ C. Dickinson,^{2,4}
 A. Barr,² R. Cepeda-Arroita,² H. C. Chiang,³ S. E. Harper,² H. M. Heilgendorff,⁵
 J. L. Jonas,^{6,7} J. P. Leahy,² J. Leech,¹ T. J. Pearson,⁴ M. W. Peel,^{8,9}
 A. C. S. Readhead,⁴ J. Sievers³

¹Sub-department of Astrophysics, University of Oxford, Denys Wilkinson Building, Keble Road, Oxford OX1 3RH, UK

²Jodrell Bank Centre for Astrophysics, Alan Turing Building, Department of Physics and Astronomy, School of Natural Sciences, The University of Manchester, Oxford Road, Manchester, M13 9PL, U.K.

³Department of Physics, McGill University, 3600 Rue University, Montréal, QC H3A 2T8, Canada

⁴Cahill Centre for Astronomy and Astrophysics, California Institute of Technology, Pasadena, CA 91125, USA

⁵Astrophysics & Cosmology Research Unit, School of Mathematics, Statistics & Computer Science, University of KwaZulu-Natal, Westville Campus, Private Bag X54001, Durban 4000, South Africa

⁶Department of Physics and Electronics, Rhodes University, Grahamstown, 6139, South Africa

⁷South African Radio Astronomy Observatory, 2 Fir Road, Observatory, Cape Town, 7925, South Africa

⁸Instituto de Astrofísica de Canarias, E-38205 La Laguna, Tenerife, Spain

⁹Departamento de Astrofísica, Universidad de La Laguna (ULL), E-38206 La Laguna, Tenerife, Spain

Accepted XXX. Received YYY; in original form ZZZ

ABSTRACT

We present a point source detection algorithm that employs the second order Spherical Mexican Hat Wavelet filter (SMHW2), and use it on C-BASS northern intensity data to produce a catalogue of point sources. The SMHW2 allows us to filter the entire sky at once, avoiding complications from edge effects arising when filtering small sky patches. The algorithm is validated against a set of Monte Carlo simulations, consisting of diffuse emission, instrumental noise, and various point source populations. The simulated source populations are successfully recovered. The SMHW2 detection algorithm is used to produce a 4.76 GHz northern sky source catalogue in total intensity, containing 1729 sources and covering declinations $\delta \geq -10^\circ$. The C-BASS catalogue is matched with the GB6 and PMN catalogues over their common declinations. From this we estimate the 90% completeness level to be approximately 630 mJy, with a corresponding reliability of 95%, when applying a Galactic mask covering 20% of the sky. We find the C-BASS and GB6/PMN flux density scales to be consistent with one another to within 3%. The absolute positional offsets of C-BASS sources from matched GB6/PMN sources peak at approximately 3.5 arcmin.

Key words: catalogues – surveys – cosmic microwave background – methods: data analysis – radio continuum: general – cosmology: observations

1 INTRODUCTION

The C-Band All-Sky Survey (C-BASS) is an experiment to observe the whole sky in total intensity and polarization at 4.76 GHz, at 45 arcmin angular resolution. The primary purpose of the experiment is to provide low-frequency data on synchrotron emission for cosmic microwave background (CMB) polarization experiments (Jones et al. 2018).

C-BASS will also provide improved measurements of low frequency emission components, enabling a detailed study of the Galactic Magnetic Field. The northern sky survey has now been completed, with detailed analysis of these data currently underway. In this paper we present a 4.76 GHz northern sky point source catalogue, produced using a point source detection algorithm employing the second-order spherical Mexican Hat Wavelet (SMHW2).

Extragalactic radio sources are a key contaminant in CMB studies, with their detection and removal being an im-

* E-mail: richard.grumitt@physics.ox.ac.uk

portant step in CMB component separation (Brandt et al. 1994; Taylor et al. 2001; Waldram et al. 2003, 2007; de Zotti et al. 2010). For future CMB experiments, it has been shown that point source contamination has the potential to significantly complicate measurements of the *B*-mode polarization power spectrum on scales $\ell \gtrsim 50$ (Mesa et al. 2002; Curto et al. 2013; Puglisi et al. 2018; Remazeilles et al. 2018). Given the large beam of C-BASS, the instrument is not well suited to point source detection, with detections of all but the brightest sources ($\gtrsim 1$ Jy) being limited by the high level of source confusion. For our C-BASS analysis, the primary data product to be obtained is a point source mask, identifying pixels contaminated by the brightest point source emission.

Numerous source detection algorithms have been developed for CMB experiments, see e.g., Tegmark & de Oliveira-Costa (1998); Vielva et al. (2003); Argüeso et al. (2009); Bennett et al. (2013); Herranz et al. (2009); Carvalho et al. (2012); López-Caniego et al. (2006); González-Nuevo et al. (2006); Planck Collaboration et al. (2014, 2016e). For our own analysis we adapt the algorithm used for *Planck* data, which employed the flat-space second-order Mexican Hat Wavelet (MHW2), using the SMHW2 to filter the whole sky. Previous applications of the first-order SMHW (SMHW1) to searches for non-gaussianity can be found in Cayón et al. (2001); Martínez-González et al. (2002); Curto et al. (2011), and to point source detection in Vielva et al. (2003). The details of this implementation are discussed in Section 3.

In addition to producing the point source mask necessary for component separation analyses, this work also allows us to perform validation checks on the C-BASS data by making comparisons with pre-existing source catalogues. In this paper we perform direct comparisons of the C-BASS catalogue with the Green-Bank 6cm (GB6) and Parkes-MIT-NRAO (PMN) 4.85 GHz catalogues (Gregory et al. 1996; Griffith & Wright 1993; Wright et al. 1994; Griffith et al. 1994, 1995; Wright et al. 1996a). By making these comparisons we are able to perform important cross-checks on the C-BASS pointing accuracy and flux density scale.

The outline of this paper is as follows: In Section 2 we summarize pre-existing source catalogues directly relevant to our C-BASS analysis. In Section 3 we discuss the C-BASS point source detection algorithm, giving an overview of the method and the Monte Carlo simulations used to validate the algorithm. In Section 4 we discuss the C-BASS total intensity, northern sky point source catalogue obtained using our detection algorithm. We compare the C-BASS catalogue with the GB6 and PMN catalogues, and calculate the differential source counts for the C-BASS sources as a cross-check on the statistical properties of the bright source population. We summarize our results in Section 5. Whilst analysis of polarized sources is important for future CMB polarization studies, this falls beyond the scope of this paper where we focus on the C-BASS total intensity results. In addition, due to the low level of source polarization, only a small number of polarized sources ($O(10)$) will be detected.

2 PRE-EXISTING SOURCE CATALOGUES

In order to construct an accurate template for masking out the point sources in the C-BASS maps it is necessary to

construct a point source catalogue based on the C-BASS observations themselves and any useful information that can be gleaned from other more sensitive, higher resolution surveys. Relevant to our work in this paper are the GB6, PMN, Effelsberg S5, RATAN-600 and CRATES catalogues (Kuehr et al. 1981; Mingaliev et al. 2007; Healey et al. 2007). These catalogues are primarily used in this paper to make comparisons with the C-BASS catalogue, for the purposes of data validation and estimation of the statistical properties of the C-BASS catalogue. However, the catalogues are also useful for characterizing the faint point source population in any C-BASS analysis (i.e., sources with flux densities below ~ 1 Jy), where reliable extraction from the C-BASS map becomes more challenging. These radio surveys are summarized in Table 1.

The GB6 and PMN 4.85 GHz source catalogues cover declinations $-87.5^\circ \leq \delta \leq 75^\circ$. The GB6 catalogue was produced using the NRAO seven-beam receiver on the 91 m telescope, and the PMN catalogue was produced using the Parkes 64 m radio telescope. The GB6 catalogue has a flux density limit of approximately 18 mJy, whilst the PMN catalogue has an average flux density limit of approximately 35 mJy over the sky (Gregory et al. 1996; Griffith & Wright 1993; Wright et al. 1994; Griffith et al. 1994, 1995; Wright et al. 1996a). The GB6 and PMN catalogues provide far deeper flux density coverage than can be achieved with C-BASS, given the differing resolutions and hence confusion levels. However, it is still necessary for us to obtain our own source catalogue, such that we can construct an accurate mask for the brightest sources in the C-BASS maps, and account for source variability between the C-BASS and GB6/PMN surveys. The GB6 and PMN catalogues remain useful in accounting for fainter sources (below ~ 1 Jy) in any C-BASS analysis.

Source catalogues covering the North Celestial Pole (NCP) region are more limited, with GB6 only covering declinations up to $\delta = 75^\circ$. The Effelsberg S5 catalogue covers declinations $\delta \geq 70^\circ$ and is complete down to 250 mJy (Kuehr et al. 1981). In comparing to the S5 catalogue there are significant issues from source variability, given the large separation in time between the S5 survey and the C-BASS survey. The RATAN-600 catalogue includes measurements at 4.8 GHz, and observed 504 sources in the NCP region with NVSS flux densities, $S_{1.4\text{GHz}} \geq 200\text{mJy}$ (Mingaliev et al. 2001, 2007). The RATAN-600 catalogue was used in a previous analysis of diffuse emission in the NCP region with C-BASS in Dickinson et al. (2019). Whilst this catalogue provides deeper flux density coverage than C-BASS, it was produced by pre-selecting sources for study from the NVSS catalogue at 1.4 GHz (Condon et al. 1998). It therefore remains an important exercise for us to carry out a blind source detection in the NCP region at 4.76 GHz.

It is also worth noting the CRATES catalogue (Healey et al. 2007). Although primarily an 8.4 GHz catalogue of bright, flat-spectrum sources covering Galactic latitudes $|b| > 10^\circ$, in Healey et al. (2009) additional observations of the NCP region at declinations, $\delta > 88^\circ$ were made to supplement the original CRATES catalogue. The purpose of this was to bring the flux density limit in this region down to the CRATES flux density limit of ~ 65 mJy. Three sources were observed in this region at 4.85 GHz, with flux densities of 67 mJy, 58 mJy and 142 mJy.

Table 1. Summary of radio surveys relevant to the work in this paper. In stating the sky coverage, δ denotes declination, and b denotes Galactic latitude.

Survey Name	Reference	Frequency [GHz]	Sky Coverage	FWHM [arcmin]	Flux Limit [mJy]	Number of Sources
C-BASS	Jones et al. (2018)	4.76	$-90^\circ \leq \delta \leq 90^\circ$ ^a	45 (60) ^b	~ 540 ^c	1729
GB6	Gregory et al. (1996)	4.85	$0^\circ \leq \delta \leq 75^\circ$	3	~ 18	75,162
PMN	Wright et al. (1996b)	4.85	$-87.5^\circ \leq \delta \leq 10^\circ$	5	~ 35	50,814
Effelsberg S5	Kuehr et al. (1981)	4.9	$70^\circ \leq \delta \leq 90^\circ$	2.7	~ 250	476
RATAN-600	Mingaliev et al. (2007)	4.8 (1.1 – 21.7) ^d	$75^\circ \leq \delta \leq 88^\circ$	0.67×6.6 ^e	(200) ^f	504
CRATES	Healey et al. (2007)	8.4 (4.85) ^g	$ b > 10^\circ$	2.4	~ 65	11,131

^a Here we state the sky coverage of the whole C-BASS experiment. The results concerning point sources in this paper were obtained for the C-BASS northern intensity data, covering declinations $-10^\circ \leq \delta \leq 90^\circ$.

^b The native resolution of C-BASS is 45 arcmin. However, the point source catalogue was produced using the C-BASS map, deconvolved and smoothed to an equivalent 1° Gaussian resolution.

^c For C-BASS we state the value $3.5\langle\sigma\rangle$, where $\langle\sigma\rangle$ is the mean background fluctuation level found across the map, applying the 20% Galactic plane mask described in Section 3.5. Details on the estimation of background fluctuation levels are given in Section 3.1.

^d The RATAN-600 catalogue covers 6 frequencies from 1.1 – 21.7 GHz, including 4.8 GHz.

^e We state $\text{FWHM}_{\text{RA}} \times \text{FWHM}_{\text{dec}}$ for RATAN-600, determined from the values given in Kovalev et al. (1999).

^f The RATAN-600 catalogue was produced by pre-selecting NVSS sources with $S_{1.4\text{GHz}} > 200$ mJy.

^g The CRATES catalogue is primarily at 8.4 GHz. However, 4.85 GHz observations were made to fill in gaps at $\delta > 88^\circ$.

3 C-BASS SOURCE DETECTION ALGORITHM

To detect sources in a sky map we need to remove obscuring diffuse emission and noise. For a source with a known point spread function (PSF) embedded in additive noise, the matched filter (MF) is the optimal filter that can be applied to maximize the source signal-to-noise ratio (SNR). The matched filter is given by,

$$\Psi_{\text{MF}}(k) = \left[2\pi \int dk k \frac{\tau^2(k)}{P(k)} \right]^{-1} \frac{\tau(k)}{P(k)}, \quad (1)$$

where k is the Fourier wavenumber, $\tau(k)$ is the source profile and $P(k)$ is the power spectrum of the unfiltered map (Tegmark & de Oliveira-Costa 1998; López-Caniego et al. 2006). However, the calculation of the MF involves a number of complications. Chiefly, we are required to make a noisy estimate of the power spectrum from our unfiltered map, and integrate it. In constructing the *Planck* Catalogue of Compact Sources (PCCS), it was found that the MHW2 achieved similar performance to the MF (López-Caniego et al. 2006; Planck Collaboration et al. 2014, 2016e). For our own analysis we adapt the *Planck* algorithm, using the SMHW2 in place of the flat-space MHW2. The SMHW2 is straightforward to calculate, enables us to filter the entire sky at once, and allows us to optimize a few free parameters as opposed to a noisy estimate of the full noise power spectrum.

3.1 Source Detection Algorithm

Given a sky map consisting of point sources, diffuse emission and instrumental noise, we can enhance the SNR of point sources in the map by filtering with the SMHW2. We perform this filtering at a range of filter scales, R to maximize the number of sources we extract from the sky maps. In changing R , we effectively change the extent to which we down-weight large scale ℓ modes that are dominated by diffuse emission, and also small scales dominated by instrumental noise. This is particularly important in regions close

to the Galactic plane where diffuse emission is very strong, meaning we must down-weight large scale modes harshly in order to extract point sources. Conversely, in regions with little diffuse emission we may wish to be less extreme in our down-weighting, so that we do not excessively reduce point source power and subsequently miss detection of fainter sources in these regions. We discuss the form of the SMHW2 filter and the effect of the filter scale, R in detail in Section 3.2.

The source detection algorithm is described below, with the algorithm flowchart displayed in Fig. 1.

(i) We begin by taking the spherical harmonic transform of our sky map, obtaining the $a_{\ell m}$ coefficients. We filter the map by weighting the $a_{\ell m}$ coefficients with the SMHW2 window function, $w_\ell^{S^2}(R)$ at some user-defined set of filter scales i.e., we calculate,

$$f_{\ell m}(R) = a_{\ell m} w_\ell^{S^2}(R). \quad (2)$$

The effect of this filtering is demonstrated in Fig. 2. Here we display a simulated sky consisting of diffuse emission, instrumental noise and point sources, along with the corresponding filtered sky with scale $R = 1$. The details of the production of this simulated sky are discussed in Section 3.3. The filter has removed diffuse emission and enhanced the SNR of point sources across the sky.

(ii) We break the maps, filtered at a range of R scales, into overlapping $10^\circ \times 10^\circ$ patches on the sky and calculate the corresponding SNR patches. We choose $10^\circ \times 10^\circ$ patches such that the flat-sky approximation holds, whilst capturing a sufficient sample of the sky background in the given sky region. We set the overlap to 5° in each direction to ensure that we obtain accurate positions for sources detected close to patch edges. The background fluctuation level in each patch is estimated by calculating the median absolute deviation (MAD) of the pixels, defined as,

$$\text{MAD}(\mathbf{X}) = \text{median} \left(|X_i - \text{median}(\mathbf{X})| \right), \quad (3)$$

where \mathbf{X} is the set of pixel values. The MAD estimator

avoids sensitivity to outlier pixel values, which can be caused by the presence of point sources in the sky patch. For each sky patch, we then select the filter scale that gives the maximal SNR for the patch.

(iii) Having selected the value of R that maximizes the patch SNR, a user-defined SNR threshold is applied to flag point sources. This produces a patch of flagged and unflagged pixels. The flagging is performed on these small, overlapping regions so as to account for the varying background properties across the sky i.e., variations in residual diffuse emission and noise.

(iv) Given our patch of flagged pixels, we then use the OPENCV Simple Blob Detector¹ to obtain source locations. The Simple Blob Detector algorithm works by applying thresholds to an input image and determining the centres of connected pixels, or sources. In addition to determining the centres of sources to sub-pixel accuracy, this software allows for the filtering of detected sources according to their geometric properties i.e., their size, circularity, convexity and inertia ratio. For our purposes, we set a maximum size limit to help prevent spurious flagging of bright diffuse emission and disallow detections within one beam FWHM of one another. For a detailed discussion of OPENCV and the Simple Blob Detector algorithm we refer the reader to [Kaehler & Bradski \(2016\)](#). The processing steps involved in studying these small sky regions are illustrated in Fig. 3, where we display the typical output from the steps outlined above.

(v) Given a set of tentative source locations obtained over the whole sky, we now repeat steps (ii) and (iii), this time centering on the tentative source locations. This step primarily helps to improve the accuracy of our source localization.

(vi) The detected source locations from all of the filtered maps are combined and duplicates are removed from the catalogue, defined here to be any reported source positions that are within the beam FWHM of one another. For matched sources in our internal catalogue, we retain the source with the greatest detected SNR.

(vii) Given the final set of source positions, source flux densities are obtained. By default, the detection pipeline obtains flux densities using aperture photometry. The aperture photometry method is adapted from [Planck Collaboration et al. \(2014\)](#); [Génova-Santos et al. \(2015\)](#). We begin by converting the map to Jy pix^{-1} , and define an aperture of radius 1 FWHM around the source position, and an annulus of inner radius 1 FWHM and outer radius 2 FWHM. The observed flux density is then given by,

$$S_{\text{obs}} = \kappa \left(S_{\text{ap}} - \bar{S}_{\text{ann}} N_{\text{ap}} \right), \quad (4)$$

where $\kappa \approx 1.1$ is a correction applied to account for flux density missing from the aperture, determined following [Planck Collaboration et al. \(2014\)](#), S_{ap} is the total flux density in the aperture, \bar{S}_{ann} is the median flux density in the annulus and N_{ap} is the number of pixels in the aperture. The uncertainty was estimated as,

$$\sigma(S_{\text{obs}}) \approx \text{MAD}(\mathbf{X}_{\text{ann}}) \frac{N_{\text{ap}}}{\sqrt{N'_{\text{ap}}}}, \quad (5)$$

where $\text{MAD}(\mathbf{X}_{\text{ann}})$ is the MAD value of pixels in the annulus

and N'_{ap} is the number of beams inside the aperture. The scaling applied to $\text{MAD}(\mathbf{X}_{\text{ann}})$ is to account for correlations in the background emission, approximately on the scale of the beam ([Génova-Santos et al. 2015](#)).

3.2 The Spherical Mexican Hat Wavelet

The Mexican Hat Wavelet (MHW) of the n^{th} kind is defined in \mathbb{R}^2 (i.e., 2-dimensional Euclidean space) as,

$$\Psi_n(\mathbf{x}, R) \propto \Delta^n \left\{ \exp\left(-\frac{|\mathbf{x}|^2}{2(R\sigma)^2}\right) \right\}, \quad (6)$$

where \mathbf{x} is the position in the image plane, Δ is the usual Euclidean Laplacian operator, σ is the Gaussian beam standard deviation and R is the filter scale factor. In changing R , we change the characteristic scale of the filter and hence the extent to which the filter down-weights large and small scale modes. Applying this expression we can arrive at the real space expression for the MHW2, given by,

$$\Psi_2(\mathbf{x}, R) \propto \left(8(R\sigma)^4 - 8(R\sigma)^2 |\mathbf{x}|^2 + |\mathbf{x}|^4 \right) \exp\left(-\frac{|\mathbf{x}|^2}{2(R\sigma)^2}\right). \quad (7)$$

In applying the MHW2 to producing the PCCS, the sky was divided up into small patches, taking flat projections and applying the MHW2 filter to them. SNR thresholding was applied to the filtered patches to extract the source positions and flux densities were then obtained for the detected sources. Here we employ the SMHW2, the equivalent of the MHW2 on S^2 (i.e., the 2-sphere). For a given filter scale, this allows us to filter the entire sky at once, avoiding complications from edge effects when filtering small patches. In dealing with a cut-sky, as with the C-BASS northern sky map, we simply apply an apodization at the edge of our mask to mitigate edge effects.

In [Antoine & Vanderghaynst \(1999\)](#) it was shown the continuous wavelet transform on S^2 can be constructed by taking the inverse stereographic projection of the \mathbb{R}^2 wavelet. This preserves the properties of the \mathbb{R}^2 wavelet and tends to the MHW in the small angle limit. The spherical MHW of the n^{th} kind is given by,

$$\Psi_{S^2}^{(n)} \propto \frac{1}{\cos^4 \frac{\theta}{2}} \Psi_n \left(|x| \equiv 2 \tan \frac{\theta}{2}, R \right), \quad (8)$$

where θ is the colatitude on the sphere ([Cayón et al. 2001](#); [Martínez-González et al. 2002](#); [Vielva et al. 2003](#); [Curto et al. 2011](#)).

Substituting the MHW2 into Equation 8, we obtain the SMHW2 as follows,

$$\Psi_{S^2}^{(2)}(\theta, R) \propto \frac{1}{\cos^4 \frac{\theta}{2}} \left[(R\sigma)^4 - 4(R\sigma)^2 \tan^2 \frac{\theta}{2} + 2 \tan^4 \frac{\theta}{2} \right] \exp\left(-\frac{2 \tan^2 \frac{\theta}{2}}{(R\sigma)^2}\right). \quad (9)$$

We normalize the SMHW2 such that we preserve point source amplitude (assuming a Gaussian PSF) after convolving it with the filter i.e.,

$$\int_{S^2} \exp\left(-\frac{|\mathbf{x}|^2}{2\sigma^2}\right) \Psi_{S^2}^{(2)}(\theta, R) \sin \theta d\theta d\phi = 1. \quad (10)$$

¹ <https://opencv.org/>

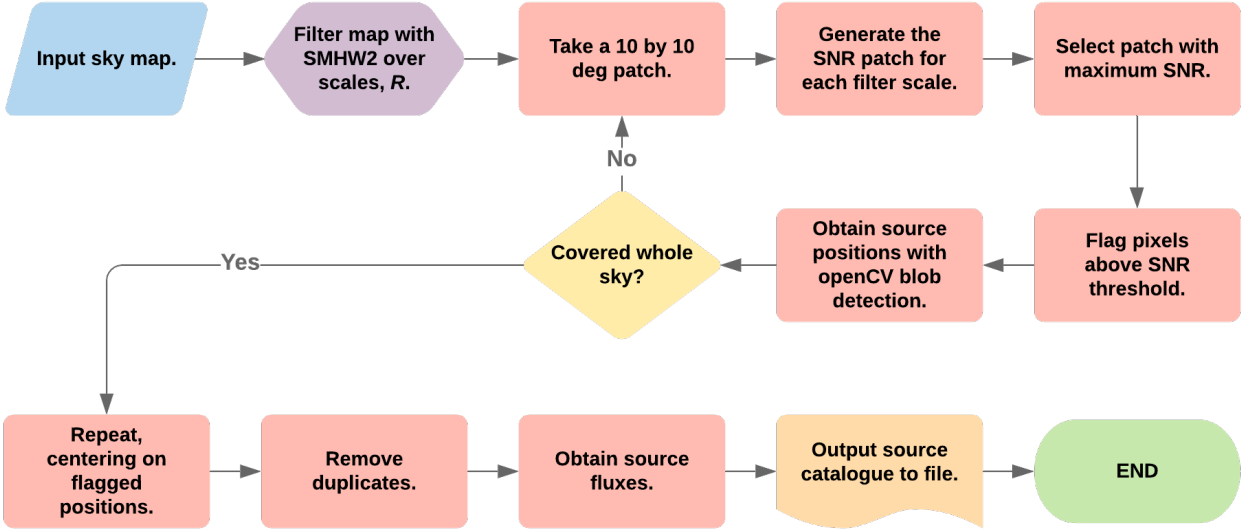


Figure 1. Flowchart for the C-BASS point source detection algorithm. The SMHW2 filter is applied over the entire sky, whilst flagging of point sources is performed on $10^\circ \times 10^\circ$ sky regions.

Given the analytic expression for the SMHW2 in real space on S^2 , we can obtain the SMHW2 window function by calculating the Legendre transform of Equation 9 i.e we calculate,

$$w_\ell^{S^2}(R) = 2\pi \int_0^\pi \Psi_{S^2}^{(2)}(\theta, R) P_\ell(\cos \theta) \sin \theta d\theta, \quad (11)$$

where $P_\ell(\cos \theta)$ is the Legendre polynomial of order ℓ .

In Fig. 4 we show the real space SMHW2 and the corresponding window function, calculated for a σ value corresponding to a FWHM of 1° , with $R = \{0.85, 0.95, 1.05, 1.15\}$. The primary effect of the SMHW2 is to down-weight large scales, which are dominated by diffuse emission. In addition to this, the SMHW2 also acts to down-weight small scale modes where instrumental noise becomes more significant. In the context of C-BASS, large-scale modes correspond to modes significantly larger than the C-BASS beam scale, $\ell \lesssim 100$, whilst small scales correspond to scales significantly smaller than the C-BASS beam scale, $\ell \gtrsim 100$.

3.3 Algorithm Validation

We validate the algorithm by running it over 100 simulations of the sky at 5 GHz. The simulated skies we generated at NSIDE=1024. This high resolution was chosen to allow for the precise determination of source positions. The simulated sky includes diffuse emission generated by PySM (Thorne et al. 2017) and an instrumental noise realization. The noise map was created by generating a Gaussian realization of the C-BASS northern-sky noise map, and calculating the power spectrum of this noise realization using the POLSPICE algorithm (Challinor et al. 2011). Given the power spectrum, we are able to generate a full-sky realization of the instrumental noise from the partial sky C-BASS noise map. This is

sufficient for the purposes of validating the algorithm performance.

To the diffuse emission simulation we add a source population to the sky. These are created by taking source flux densities from the PMN, GB6 and RATAN-600 surveys, and scattering the sources at random positions over the sky (Gregory et al. 1996; Griffith & Wright 1993; Wright et al. 1994; Griffith et al. 1994, 1995; Wright et al. 1996a; Mingaliev et al. 2007). Carrying this out 100 times we obtain 100 Monte Carlo simulations of the sky, consisting of the same diffuse and noise background but with their source populations randomly distributed on the sky. The simulated skies are all smoothed to a 1° Gaussian to match the deconvolved and smoothed C-BASS maps.

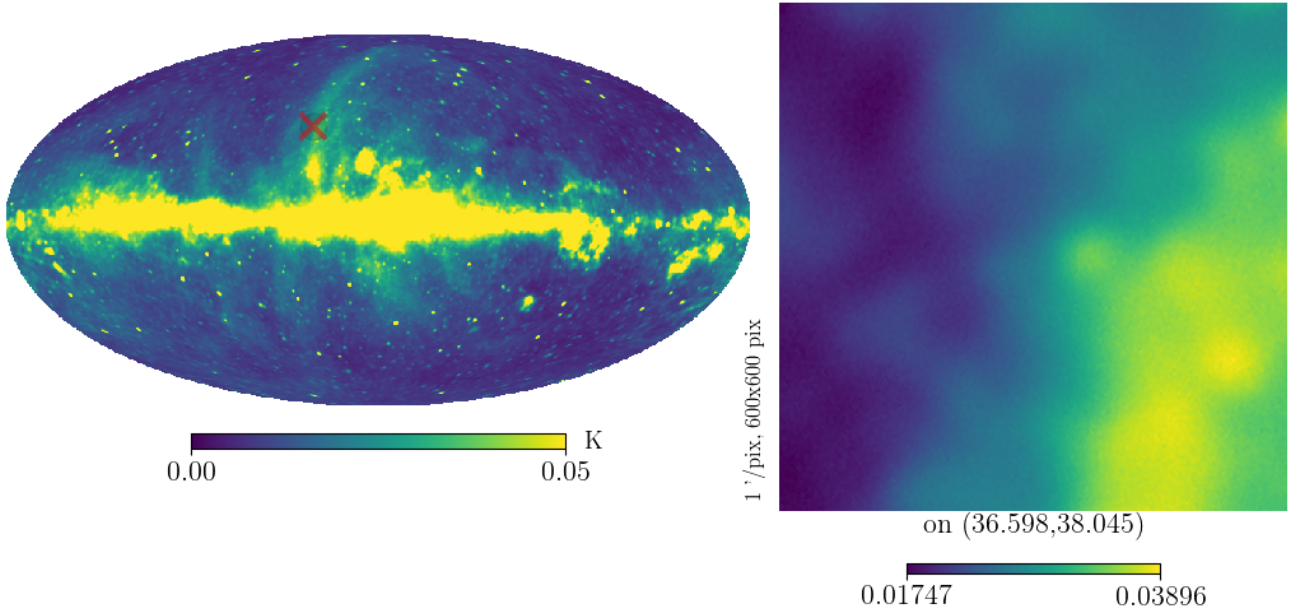
The diffuse components included in the simulation are as follows:

(i) **Synchrotron Radiation** - This was generated using the re-processed 408 MHz Haslam map (Remazeilles et al. 2015) as a template and scaled using a spectral index and curvature model. This corresponds to the PySM s3 model.

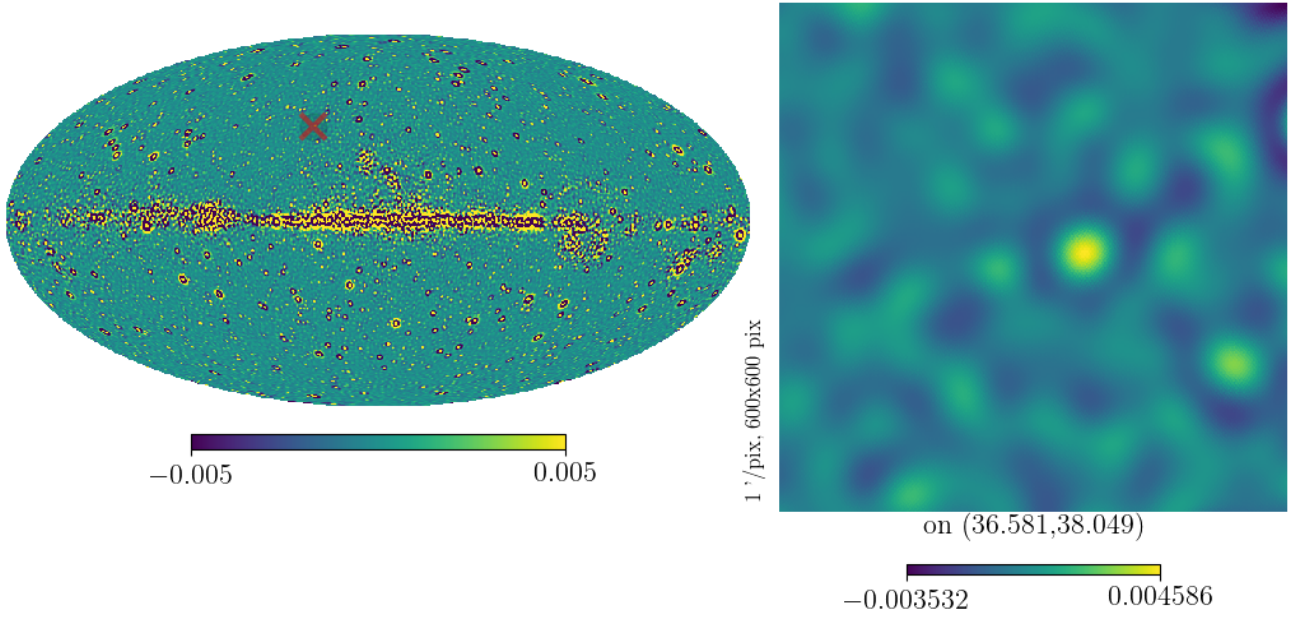
(ii) **Free-Free Emission** - This was generated with the analytic model used in the *Planck* COMMANDER analysis (Draine 2011; Planck Collaboration et al. 2016d,c). The free-free template is scaled using a single power-law. This corresponds to the PySM f1 model.

(iii) **Anomalous Microwave Emission (AME)** - This was generated by modelling emission caused by the sum of two spinning dust populations. Scaling is calculated using the SPDUST2 code (Ali-Haïmoud et al. 2009). This corresponds to the PySM a2 model.

(iv) **Thermal Dust** - This was generated by modelling the emission caused by a single modified black body. This corresponds to the PySM d1 model (Planck Collaboration et al. 2016d).



(a) Input sky



(b) Filtered sky

Figure 2. In panel (a) we show an input 5 GHz simulated sky consisting of diffuse emission generated using PYSM, instrumental noise generated from a realization of the C-BASS northern-sky noise map power spectrum, along with a point source population generated by scattering the GB6, PMN and RATAN-600 sources at random positions over the sky. Alongside this we display a zoom-in centered on the location of the red cross on the map. In panel (b) we show the same map after being convolved with the SMHW2 filter, removing the large scale diffuse emission and leaving behind a sky filled with point sources. As before, we display a zoom-in of the filtered map alongside it, centred on the location of the red cross. It is important to note here that not all the diffuse emission has been removed at low galactic latitudes. In regions of strong diffuse emission the source detection algorithm is significantly less reliable. In panel (b) it is apparent that the SMHW2 filtering produces sidelobes around sources. Whilst this can lead to issues with spurious flagging of sidelobe peaks, this is only found to be a problem around the brightest sources on the sky i.e., those with flux densities $\gtrsim 100$ Jy. This problem can largely be side-stepped by allowing for larger exclusion zones around the brightest sources, as was the case with catalogues such as GB6, and masking larger sky areas around the brightest sources accordingly.

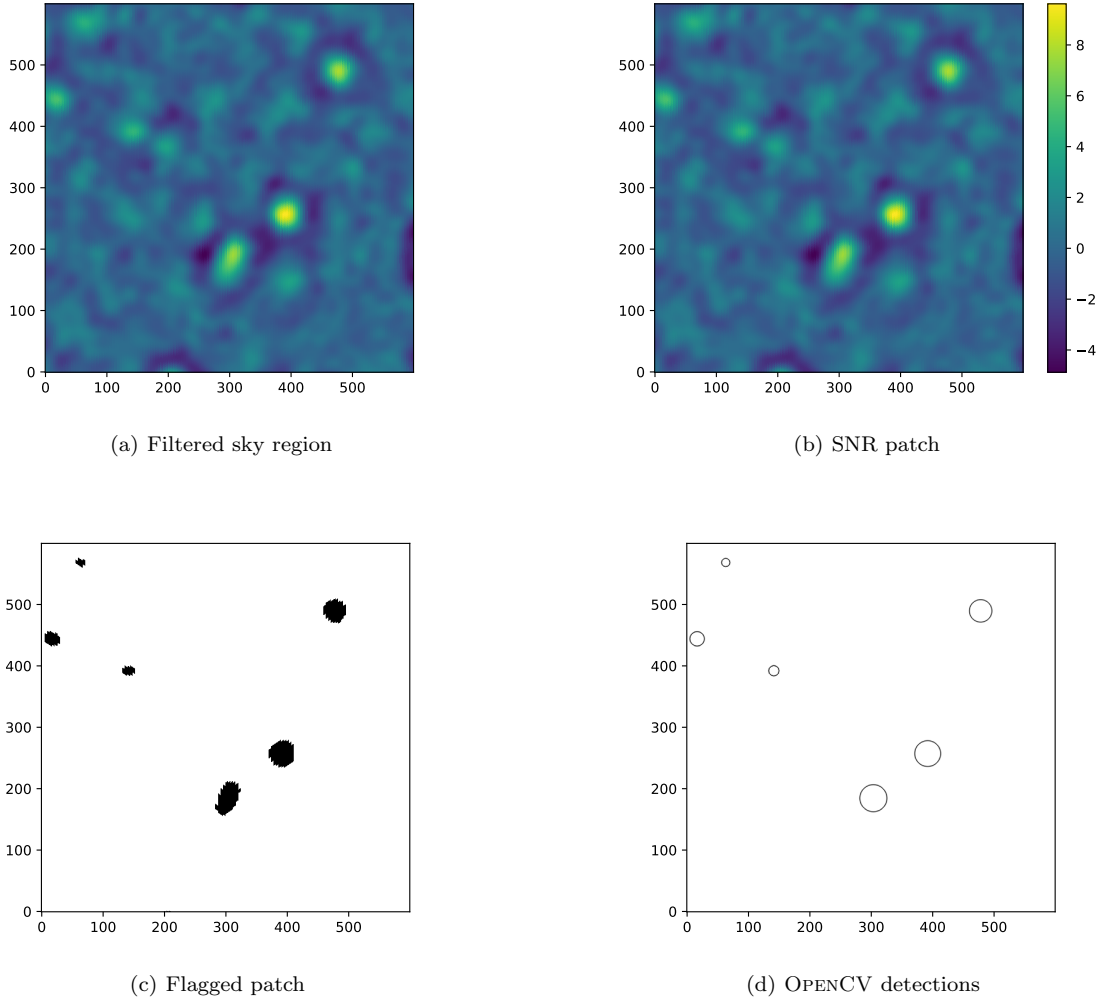


Figure 3. Images illustrating the flagging process. In panel (a) we show a projection of a filtered map, produced by convolving a simulated sky map with the SMHW2. Given a filtered patch, we produce a SNR patch, using the median absolute deviation of the patch values as the indicative noise value. This results in a patch as shown in panel (b). We then apply a $\text{SNR} \geq 4$ threshold to produce a binary patch of flagged and un-flagged pixels as shown in panel (c). In this case, flagged pixels are *black* and un-flagged pixels are *white*. This binary patch is then passed to the OPENCV Simple Blob Detector, which identifies the central positions of flagged sources in the image. The detected locations for the simulated patch here are shown in panel (d) as circles centred on the detected source locations.

(v) **CMB** - A lensed CMB realisation was generated using the Taylens code (Naess & Louis 2013), as part of PYSM. This corresponds to the PYSM c1 model.

One of the simulated skies is shown in Fig. 2, along with the same sky filtered at the scale $R = 1$. After running our detection algorithm over the simulated skies, we compare the detected sources to our input catalogues. From this, we calculate the completeness level of our detected sources, averaged over all the simulations, and record the absolute deviations of detected sources from their true positions. The validation results are presented in Section 3.5, produced using a detection threshold of $\text{SNR} \geq 4$ i.e., we flag pixels in sky patches with $\text{SNR} \geq 4$. This was selected to give a catalogue reliability of approximately 90 to 95% when masking 20% of the sky around the Galactic plane. Here we define catalogue completeness as the fraction of sources above some given flux density threshold that are recovered by the de-

tection algorithm. The catalogue reliability is defined as the fraction of detected sources that are matched with at least one source in the input catalogue.

3.4 Catalogue Matching: Likelihood Ratios

The simulated validation catalogue is produced for a map with a resolution of 1° . Given the large number of sources used for our input catalogue, source confusion presents a major complication when trying to match the output catalogues with the corresponding input catalogues from our Monte Carlo simulations. One source in the output catalogue will likely result from the blending of multiple sources in the input catalogue, and a single source in the input catalogue can contribute to more than one source in the output catalogue. We face identical issues when matching the real

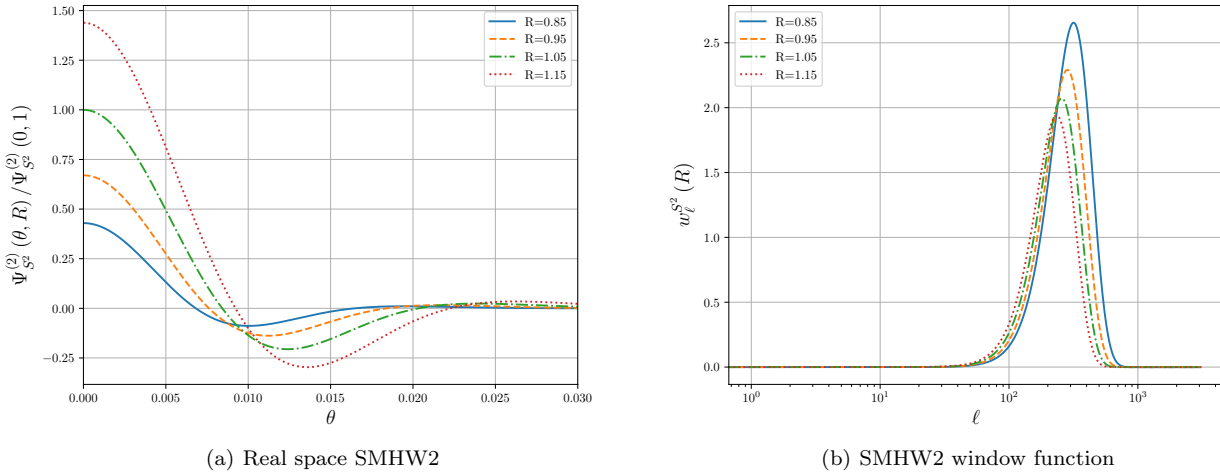


Figure 4. The real space SMHW2 (left) and corresponding window functions (right), shown for σ corresponding to a FWHM of 1° and $R \in \{0.85, 0.95, 1.05, 1.15\}$. The SMHW2 down-weights large and small scales, with changes in R determining the severity with which we down-weight large and small scale emission.

C-BASS catalogue to higher resolution catalogues such as GB6 and PMN.

To find matches between our input and output catalogues we use a likelihood ratio test. This has previously been used in matching point source catalogues, particularly when dealing with problems from source confusion, see e.g., Richter (1975); Sutherland & Saunders (1992); Mann et al. (1997); Rutledge et al. (2001); Chapin et al. (2011); Wang et al. (2014). The core of the likelihood ratio test consists in calculating the ratio of the probability of a match between an input and output source being a true match, to the probability of the match being a random association. The likelihood ratio is given by,

$$\text{LR} = \frac{q(\Delta S_f) f(r)}{2\pi r \rho(\Delta S_f)}, \quad (12)$$

where $q(\Delta S_f)$ is the probability density function (PDF) for a given match being a true match as a function of the fractional flux density difference (ΔS_f) between the two sources, $f(r)$ is the PDF for true matches as a function of the absolute positional offset between the two sources, r , $2\pi r$ is the PDF for random associations assuming a uniform spatial distribution of background sources, and $\rho(\Delta S_f)$ is the PDF for random associations as a function of ΔS_f .

For the positional PDF of true input-output matches, we assume a Gaussian distribution over the orthogonal coordinate axes. This gives a Rayleigh distribution for the PDF of true input-output matches as a function of r i.e.,

$$f(r) = \frac{r}{\sigma_r} \exp\left(-\frac{r^2}{2\sigma_r^2}\right), \quad (13)$$

where σ_r is a scaling parameter. The position and flux density PDF parameters are estimated by comparing our output source catalogues with the corresponding input catalogues. We determine $f(r)$ by searching for all candidate matches between the input and output catalogues, using a search radius of 1° around each output source. Candidate matches

will consist of true input-output matches, along with random background associations. Assuming a uniform distribution of background sources the random matches will follow a linear trend, scaling with the sky area enclosed by a given search radius. We therefore fit $f(r)$ plus a linear trend to the histogram of absolute positional offsets for candidate input-output matches to obtain an estimate for $f(r)$.

To determine $\rho(\Delta S_f)$, we generate randomized output catalogues by randomly distributing our output sources over the sky and randomly swapping source flux densities. We then find candidate matches between input and randomized output sources, again using a 1° search radius. We bin the candidate matches as a function of the fractional flux density difference between the input and output source, given by,

$$\Delta S_f = \frac{S_{\text{out}} - S_{\text{in}}}{S_{\text{in}}}, \quad (14)$$

where S_{out} is the output source flux density and S_{in} is the input source flux density. This gives us the number of random matches as a function of ΔS_f and hence our estimate for $\rho(\Delta S_f)$. To obtain $q(\Delta S_f)$ we carry out the same procedure as above, but with the real output catalogues. We then estimate $q(\Delta S_f)$ from the difference between the number of matches as a function of ΔS_f for the real output catalogues, and the number of matches for the randomized catalogues i.e., from the excess matches in the real output catalogues.

To determine the LR threshold for declaring a true match we calculate the likelihood ratios for all candidate matches between the input catalogues and randomized output catalogues. From this we determine the value of LR at which we would declare 10% of our randomized matches to be true matches. This value is used as the LR threshold at which we declare a true input-output match. This is sufficient for limiting the fraction of false identifications with the input catalogue, whilst ensuring a low probability of spuriously identifying a source in the output catalogue as a true positive, given that matched output sources are typically associated with multiple input sources.

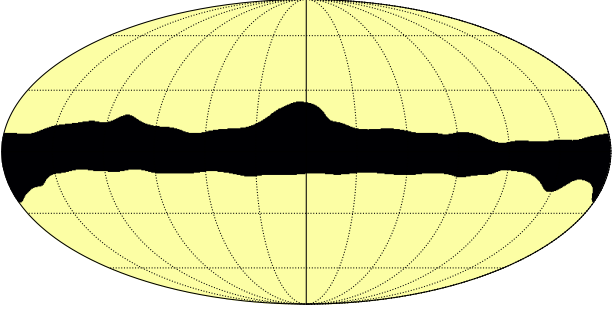


Figure 5. The Galactic plane mask used in our analysis of the C-BASS catalogue, covering 20% of the sky. The mask was taken from the Galactic emission masks used in the *Planck* analysis. Masked regions are shown in black (Planck Collaboration et al. 2016b,a).

3.5 Validation: Completeness, Position and Flux Density Accuracy

We obtain the catalogue completeness and reliability, averaged over our Monte Carlo simulations, to confirm the ability of the source detection algorithm to accurately recover an input source population.

When masking the sky, we use the Planck 2015 Galactic plane mask covering 20% of the sky² (Planck Collaboration et al. 2016b,a). The mask is shown in Fig. 5. In determining the positional offset of the detected source from the input sources, we compare its position to the photocentre of matched input sources. That is, after matching to input sources using the LR test, we determine the weighted average position of the matched input sources, using the input source flux densities as weights. In comparing flux densities, we sum matched source flux densities, weighted according to the beam profile for a 1° Gaussian i.e.,

$$S_v^{\text{match}} = \sum_i S_v^{(i)} \exp \left\{ -\frac{(\mathbf{x}_i - \mathbf{x}_{\text{det}})^2}{2\sigma^2} \right\}, \quad (15)$$

where the sum runs over matched sources in the input catalogues, $S_v^{(i)}$ is the flux density of the i^{th} matched source, \mathbf{x}_i is the position of the i^{th} matched source, \mathbf{x}_{det} is the position of the detected source and σ is the beam standard deviation.

We show the catalogue completeness curves in Fig. 6. When we apply a Galactic mask, the catalogue completeness level improves. This is to be expected given the reduced levels of diffuse emission as we only consider regions away from the Galactic plane. With no Galactic Plane mask we obtain a 90% completeness level of approximately 840 mJy, with a catalogue reliability of approximately 78%. Applying a Galactic plane mask over 20% of the sky, we obtain a 90% completeness level of approximately 550 mJy, corresponding to a catalogue reliability of approximately 92%.

² The mask was downloaded from the Planck Legacy Archive: <https://pla.esac.esa.int/>. The full filename is HFI_Mask_GalPlane-apo0_2048_R2.00.fits.

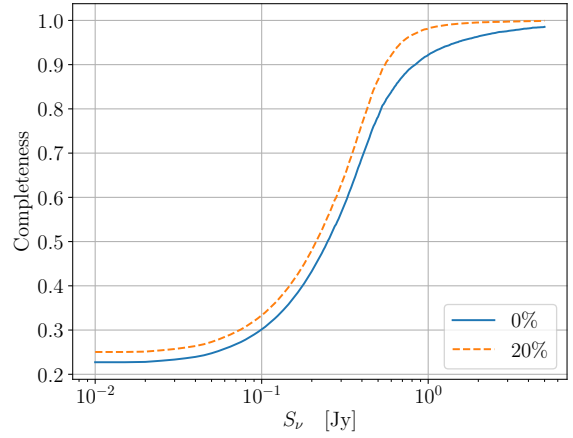


Figure 6. The validation catalogue completeness as a function of flux density, obtained from running the SMHW2 algorithm over 100 simulated skies. The catalogue completeness is displayed for Galactic plane masks covering 0% and 20% of the sky. Applying a 20% Galactic plane mask, we achieve 90% completeness at approximately 550 mJy.

The absolute positional offsets of detected sources in the validation simulations clusters below 10 arcmin, peaking around 1.2 arcmin. Considering the 1° resolution of the maps used for source detection, and the significant confusion effects at this resolution, this is a small positional uncertainty for our source detection algorithm. Indeed, for the purposes of producing a point source mask for the actual C-BASS maps this is more than sufficient. The histogram of absolute positional offsets of detected sources, applying a 20% Galactic plane mask, is shown in Fig. 7.

We are able to recover input source flux densities using aperture photometry, with a plot of detected flux densities against input flux densities being shown in Fig. 8. At flux densities greater than 1 Jy we recover reasonable flux density estimates for the majority of sources. A small fraction of sources are recovered with flux densities biased slightly high. This is to be expected given the 1° resolution of the C-BASS map used in source detection, meaning that multiple input sources are associated with each detected source. The detected source flux density will be the summed contribution from associated input sources, some of which may fail the likelihood ratio test during source matching. For flux densities below ~ 1 Jy the scatter in the recovered flux densities reaches the same magnitude as the input flux densities. This is again to be expected; below this level sources become much more heavily obscured by surrounding diffuse emission, making photometric estimates of source flux densities significantly more unreliable. We note here that there is a small cluster of recovered sources at these low flux densities where the recovered flux density estimate is spuriously high. This is largely caused by sources being detected in regions of bright diffuse and blob-like emission, leading to errors in the background estimation.

Our validation simulations have demonstrated that our source detection algorithm is able to accurately recover an

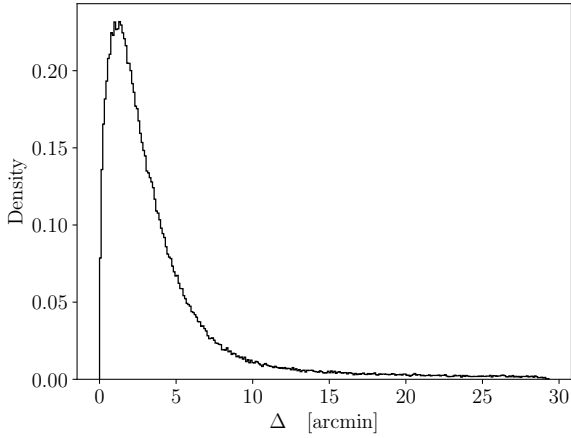


Figure 7. The histogram of detected positional offsets, applying a 20% Galactic plane mask, obtained for the 100 Monte Carlo simulations. Over the un-masked sky area we find the detected positional offsets peak at approximately 1.2 arcmin, clustering below 10 arcmin.

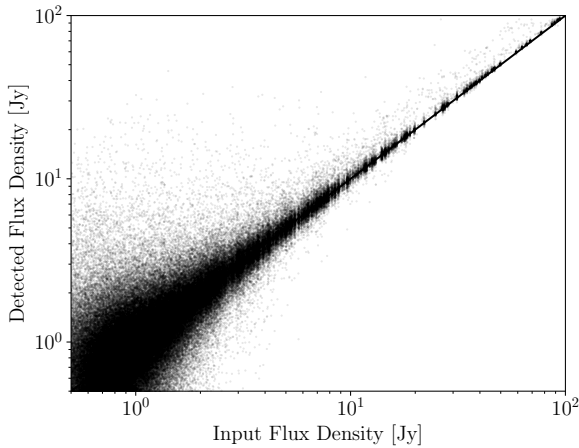


Figure 8. The detected flux densities against matched input flux densities, applying a 20% Galactic plane mask, obtained for the 100 Monte Carlo simulations. For the majority of sources above 1 Jy we recover reasonable flux density estimates.

underlying source population, from a sky consisting of additional contributions from diffuse emission and noise.

4 THE C-BASS NORTHERN SKY CATALOGUE

In this section we present the C-BASS northern sky, total intensity point source catalogue. The point source catalogue was produced using nighttime only, all elevations data. That is, the data was obtained from nighttime observations, combining data from the various elevation scans of the telescope. C-BASS data were calibrated against Tau A as a primary calibrator and Cas A as a secondary calibrator, with calibra-

tor flux densities being calculated from the spectral forms in Weiland et al. (2011). The C-BASS calibration is accurate to $\sim 5\%$. Detailed discussions of the C-BASS data reduction and calibration will be given in the C-BASS survey and commissioning papers (Taylor et al., in prep. and Pearson et al., in prep). We perform the source detection on the C-BASS map at NSIDE=1024, using the high NSIDE map to allow for the precise determination of source positions. The source detection was performed on the C-BASS map which had been deconvolved and smoothed to an effective Gaussian resolution of 1° , such that we matched the map used in other scientific analyses with C-BASS, see e.g., Dickinson et al. (2019).

The outline of this section is as follows: In Section 4.1 we summarize the catalogue properties. In Section 4.2 we present the results from matching the C-BASS and GB6/PMN catalogues, using these results to quantify the C-BASS pointing accuracy and flux density scale. In Section 4.3 we comment briefly on sources detected with outlier flux densities. In Section 4.4 we show the differential source counts for the C-BASS catalogue, and compare these to the GB6 source counts. Additional comparisons were also made with sources in the RATAN-600 catalogue over the NCP region. In this case we recovered the expected bright source population, with the results obtained through these comparisons being consistent with those from comparisons with the GB6/PMN catalogues.

4.1 Northern Sky Intensity Catalogue: Summary

For our default catalogue, we run the source detection algorithm using a detection threshold of $\text{SNR} \geq 3.5$. Whilst we found a threshold of $\text{SNR} \geq 4$ to be appropriate during algorithm validation, we found that we could reduce the SNR threshold for producing the real catalogue whilst still maintaining a high catalogue reliability. To estimate the completeness and reliability of the real C-BASS catalogue we compare it with the GB6 and PMN catalogues over their common declinations. Applying a Galactic plane mask covering 20% of the sky we obtain a catalogue reliability of approximately 95%, with a corresponding 90% completeness level of 630 mJy, recovering the expected bright source population at 4.76 GHz. The confusion level for our 1° smoothed C-BASS maps can be estimated following Condon (1974); Meyers et al. (2017), and is given by,

$$\sigma_c \approx 0.2 \left(\frac{\nu}{\text{GHz}} \right)^{-0.7} \left(\frac{\theta_{\text{FWHM}}}{\text{arcmin}} \right)^2 \approx 240 \text{ mJy beam}^{-1}. \quad (16)$$

Below this level sources cannot be individually detected in our maps, acting as an additional noise contribution. Our analysis has resulted in a catalogue of 1729 point sources covering declinations $\delta \geq -10^\circ$. The catalogue properties are summarized in Table 2, with the detected source positions for the default catalogue shown in Fig. 9.

It is important to note here that, whilst there are a large number of source detections in the Galactic plane, the reliability of these detections is significantly lower than at higher Galactic latitudes. This is a result of the more intense diffuse emission obscuring point sources, and blob-like emission in the galaxy being spuriously identified as point sources. For the purposes of scientific analyses with other CMB datasets

Table 2. C-BASS northern sky, total intensity catalogue summary. Position uncertainties include intrinsic uncertainty from the source detection algorithm, along with additional errors from the C-BASS pointing.

C-BASS Catalogue	
Frequency	4.76 GHz
Map FWHM ^a	1°
SNR threshold.....	3.5
Reliability:	
Full Sky	87%
20% Galactic mask	95%
Number of sources:	
Full sky	1729
20% Galactic mask	1258
90% completeness:	
Full sky	1900 mJy
20% Galactic mask	630 mJy
$N(S > S_{90})^b$:	
Full sky	493
20% Galactic mask	728
Position uncertainty	
Full sky	3.7 arcmin
20% Galactic mask	3.5 arcmin

^a The 1° map FWHM corresponds to the C-BASS map that has been deconvolved from the C-BASS beam and smoothed to a 1° Gaussian.

^b This is the number of sources with measured flux densities greater than the 90% completeness level.

this is not a major issue, given that much of the Galactic plane will be masked out for such analyses anyway.

4.2 GB6 and PMN Matching

To cross-check the C-BASS pointing and flux density scale, we match the C-BASS point sources with the GB6 catalogue over the common declinations $0^\circ \leq \delta \leq 75^\circ$, and with the PMN catalogue over $-10^\circ \leq \delta \leq 10^\circ$. Similar to the situation encountered during the algorithm validation, the GB6 and PMN catalogues were produced using much higher resolution surveys than C-BASS. What may appear as a single source in the C-BASS maps could actually correspond to multiple sources in the GB6 and PMN catalogues. Matches between catalogues are found using the likelihood ratio technique described in Section 3.4. In characterizing the C-BASS pointing, we compare the C-BASS source position with the photocentre of matched GB6 or PMN sources. In comparing flux densities we use the beam weighted sum of matched source flux densities.

In Fig. 10 we show a histogram of the absolute positional offsets of C-BASS sources from matched GB6 and PMN sources, using the photocentres of matched GB6 and PMN sources for comparison. The offsets are clustered below 10 arcmin, peaking at approximately 3.5 arcmin³. This is broadly consistent with the results obtained from our Monte Carlo simulations during the algorithm validation, with additional errors arising here from the C-BASS pointing. In-

³ Note that the position of the mode for a Rayleigh distribution is given by σ_r .

deed, the peak positional offset obtained here is consistent with the residuals obtained from C-BASS pointing measurements (Muchovej et al., in prep.). The distributions of the absolute positional offsets when matching to GB6 and PMN are also very similar. The lack of large positional offsets in the C-BASS catalogue provides a useful confirmation of the C-BASS pointing accuracy.

We also plot the C-BASS source flux densities (determined using aperture photometry) against matched GB6 and PMN flux densities, using Equation 15 to determine the matched flux density, in Fig. 11. When no Galactic plane mask is applied, we can see that most sources cluster around the line $S_v^{GB6} = S_v^{CBASS}$ ($S_v^{PMN} = S_v^{CBASS}$). However, there is an apparent population of sources where the measured C-BASS flux density is significantly greater than the GB6 and PMN flux densities. This is largely due to the flagging of sources in the Galactic plane, where the additional presence of very bright, blob-like emission leads to spuriously high flux density estimates. On applying a Galactic plane mask this population is largely removed. The small number of remaining sources where C-BASS significantly over-estimates the flux densities may either result from sources sitting in regions of bright diffuse emission (e.g., within a Galactic spur) or from heavily confused sources in the C-BASS map. Most of the sources recovered with spuriously high densities are associated with low flux density GB6/PMN sources ($\lesssim 1$ Jy). At these flux densities the uncertainties in our flux density estimates from aperture photometry become much larger, consistent with the larger spread in C-BASS to matched flux densities at these levels.

To quantify the agreement between the C-BASS and GB6/PMN flux density scales we study the ratios of matched source flux densities, and fit for the average flux density ratio using a Gaussian mixture model. This allows us to model the outlier population that results from detections in bright sky regions. The likelihood is given by a weighted sum of Gaussians,

$$p(\mathcal{R}|w) \propto w\mathcal{N}(\mathcal{R}|\mu_{in}, \sigma_{in}) + (1-w)\mathcal{N}(\mathcal{R}|\mu_{out}, \sigma_{out}), \quad (17)$$

where \mathcal{R} is the flux density ratio for matched sources, μ_{in} and σ_{in} define the mean and spread of flux density ratios for the inlier population, μ_{out} and σ_{out} define the mean and spread of flux density ratios for the outlier population, and w gives the proportion of points corresponding to the inlier population. We assign priors to our parameters as follows,

$$\mu_{in} \sim \mathcal{N}(\mu = 1, \sigma = 0.25), \quad (18)$$

$$\sigma_{in} \sim \text{Exp}(\lambda = 2), \quad (19)$$

$$\mu_{out} \sim \mathcal{N}(\mu = 2, \sigma = 0.5), \quad (20)$$

$$\sigma_{out} \sim \text{Exp}(\lambda = 1), \quad (21)$$

$$w \sim \text{Beta}(1/2, 1/2). \quad (22)$$

We select weakly informative priors for the Gaussian population parameters and assign a Beta prior to w , $p(w) \sim \text{Beta}(1/2, 1/2)$, which corresponds to the Jeffreys prior for a Binomial distributed random variable (Jeffreys 1961). We sample our model using the No-U-Turn Sampler (NUTS), implemented in PyMC3 (Hoffman & Gelman 2014; Salvatier et al. 2016). NUTS is a self-tuning variant of Hamiltonian Monte Carlo that allows for highly efficient exploration of the parameter space.

The results for our fitted values of μ_{in} , comparing to

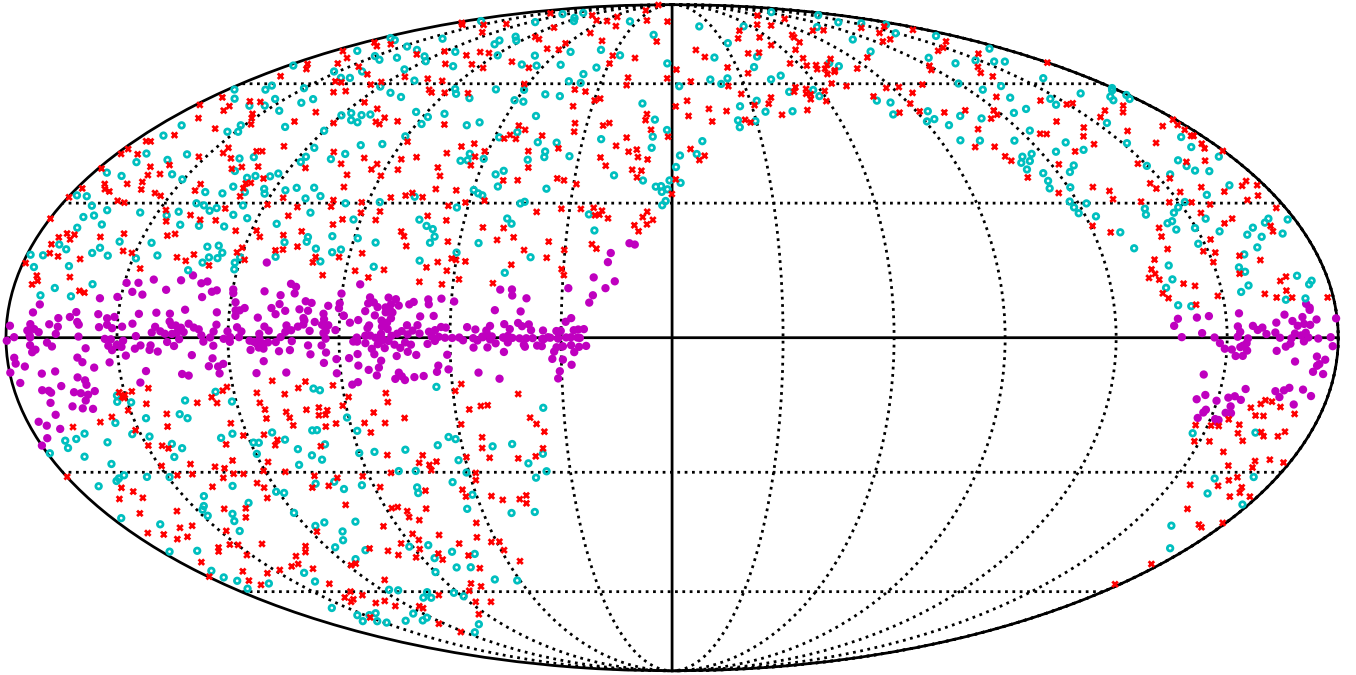


Figure 9. Positions of the northern sky, total intensity C-BASS point sources. Positions shown here are in Galactic coordinates. *Filled purple circles* denote sources that fall within the 20% Galactic plane mask. *Open cyan circles* denote sources outside the mask, with a fitted flux density below the 90% completeness level (630 mJy), and *red crosses* denote the remaining sources with fitted flux densities above the 90% completeness level.

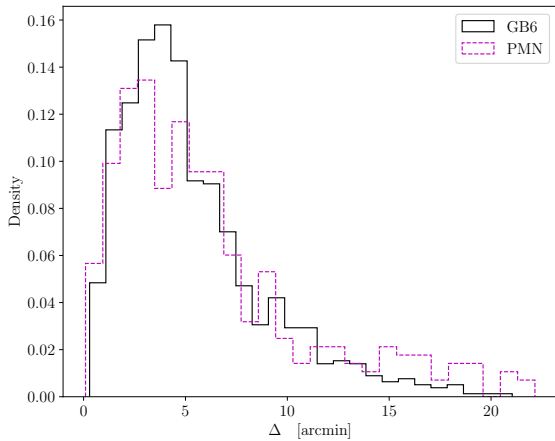


Figure 10. A histogram of the absolute positional offsets of C-BASS sources from matched GB6 and PMN sources, applying a 20% Galactic plane mask. We use the photocentres of matched GB6 and PMN sources for comparison. Positional offsets cluster below 10 arcmin, peaking at approximately 3.5 arcmin. We obtain similar distributions for the absolute positional offsets with both GB6 and PMN.

GB6 and PMN, are given in Table 3. The C-BASS flux density scale is consistent with the GB6/PMN flux density scales to within $\sim 3\%$. We note here that the fitted values μ_{in} are largely independent of the Galactic plane mask being applied. This is simply a result of the Gaussian mixture

Table 3. Fitted values for μ_{in} . Values were obtained by comparing flux density ratios between C-BASS and GB6/PMN, applying 0% and 20% Galactic plane masks. Alongside the mean fitted value for μ_{in} , we also give the 95% highest posterior density (HPD) interval. The C-BASS and GB6/PMN flux densities are found to be consistent to within $\sim 3\%$.

Comparison Catalogue	$\langle \mu_{\text{in}} \rangle$	95% HPD[μ_{in}]
GB6 0% mask	0.99	{0.96, 1.02}
GB6 20% mask	0.97	{0.93, 1.00}
PMN 0% mask	1.00	{0.95, 1.07}
PMN 20% mask	1.01	{0.95, 1.08}

model accounting for the outlier population, which is much more significant when no Galactic plane mask is applied. Differences between the flux density scales will result from a number of complicating factors e.g., the fact that C-BASS sources are really blends of multiple GB6/PMN sources, differing pass-bands, source variability etc. Given this, and the additional $\sim 5\%$ uncertainties in the GB6 and PMN flux density scales, we conclude that the C-BASS flux density scale is consistent with these flux density scales (Gregory et al. 1996; Griffith & Wright 1993; Wright et al. 1994; Griffith et al. 1994, 1995; Wright et al. 1996a). We do not include any colour corrections in this analysis. The choice of 4.76 GHz as the effective frequency for C-BASS minimizes colour corrections to $\sim 1\%$, meaning any corrections in extrapolating flux densities from 4.76 GHz to 4.85 GHz will have negligible impact on the analysis presented here.

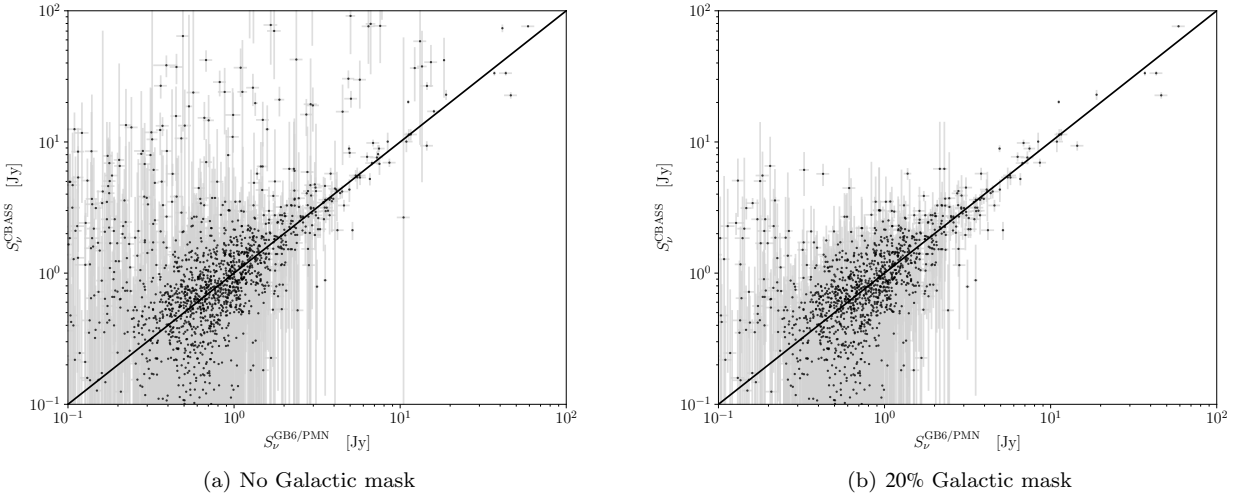


Figure 11. Flux-flux plots for matched C-BASS and GB6/PMN sources. In panel (a) we plot sources with no Galactic mask applied, and in panel (b) we apply a 20% Galactic mask. We also plot the line $S_{\nu}^{\text{GB6/PMN}} = S_{\nu}^{\text{CBASS}}$ in each panel. When we do not apply a Galactic mask, we can see a group of C-BASS sources with significantly higher flux densities than the matched GB6/PMN sources. This can be attributed to errors in fitting for source flux densities in the Galactic plane, particularly in the presence of bright blob-like emission. On applying a Galactic plane mask, this group of sources is largely removed and sources cluster more tightly around $S_{\nu}^{\text{GB6/PMN}} = S_{\nu}^{\text{CBASS}}$.

4.3 Outlier Sources

Pauliny-Toth et al. (1978) showed that approximately 60% of strong radio sources at 5 GHz have flat spectra and are therefore likely to be compact, variable sources. Indeed, previous studies of the GB6 source catalogue have found a significant fraction of variable sources (Gregory et al. 1996, 1998, 2001). As such, we would expect roughly half of the objects in 5 GHz surveys to be varying, meaning any comparison of individual flux densities observed at different epochs will be strongly contaminated by source variability. Even so, a comparison of flux densities over the whole catalogue remains useful for checking the overall consistency of the different flux density scales, and for identifying any extreme differences that could be the result of systematic errors or due to interesting astrophysical variations.

In this section, we have extracted all sources that show at least a 5σ discrepancy between the C-BASS and GB6 flux densities, when applying a 20% Galactic plane mask. Doing this, we find six outlier sources in the C-BASS catalogue. For two of these sources, they consist of detections near a very bright neighbouring source. In this situation the background estimation during aperture photometry is likely to break down, leading to an unreliable estimate of the flux density. In another case, bright blob-like diffuse emission was flagged which was subsequently matched with nearby GB6 sources. More generally, the blending of sources by diffuse emission and confusion with other sources can lead to aperture photometry becoming unreliable. This is particularly true at flux densities below ~ 1 Jy.

However, as is to be expected at this frequency there is clear evidence of variability. In Table 4 we summarise the measured properties of the three 5σ outliers in the C-BASS catalogue that are not the obvious result of confusion or blending by diffuse emission, along with source identifications. These sources were relatively isolated, with seemingly

little contribution from diffuse emission and source confusion. The three sources are all active galaxies, which are known to exhibit long term variability. The levels of variation we observe here, at a factor of ~ 2 , are consistent with previous observations of AGN variability at radio frequencies (Ulrich et al. 1997; Hovatta et al. 2008). In the case of 3C 84, a large flare-up in the flux density at cm wavelengths was observed during the 1980s, with subsequent decreases of ~ 10 Jy into the 2000s. This is consistent with the large magnitude decrease in the flux density we note between the GB6 and C-BASS surveys (Nagai et al. 2012). A detailed study of source variability between the C-BASS and GB6/PMN catalogues is beyond the scope of this paper, but there is evidence that source variability accounts for some of the flux density discrepancies between the C-BASS and GB6/PMN catalogues.

4.4 Differential Source Counts

Differential source counts have been intensively studied, having important implications for models of cosmic evolution and provided the first clear evidence against the Steady State Theory (Pooley & Ryle 1968; Condon 1984; de Zotti et al. 2005, 2010; Massardi et al. 2010; AMI Consortium et al. 2011). However, for the purposes of C-BASS analysis we calculate the differential source counts to provide an additional cross-check on the statistical properties of our bright source population.

Given that we are concerned with the statistical properties of our catalogue at flux densities $\gtrsim 1$ Jy, where the C-BASS catalogue is largely complete, we do not consider correction factors to the differential source counts necessary at lower flux densities to account for catalogue incompleteness and varying flux density sensitivities across the sky. The C-BASS differential source counts are determined following

Table 4. In this table we summarise the source properties of $\geq 5\sigma$ outliers in the C-BASS catalogue, that show evidence for source variability between the C-BASS and GB6 surveys.

RA	DEC	S_{CBASS} [Jy]	S_{GB6} [Jy]	$S_{\text{CBASS}}/S_{\text{GB6}}$	Source ID	Object Type
03 ^h 19 ^m 43 ^s	+41°31'46"	22.7 ± 1.3	46.3 ± 4.1	0.5 ± 0.1	3C 84	Seyfert 2 Galaxy
23 ^h 38 ^m 52 ^s	+26°58'04"	3.9 ± 0.4	1.7 ± 0.1	2.3 ± 0.3	3C 465	Seyfert 1 Galaxy
12 ^h 24 ^m 50 ^s	+21°22'49"	2.9 ± 0.3	1.1 ± 0.1	2.6 ± 0.4	QSO B2136+1410	Quasar

the method in [Riseley et al. \(2016\)](#). Sources are put into flux density bins of width 0.3 dex. For each bin, source counts are determined against a central flux density, S_c , taken to be the geometric mean of flux densities in that bin. The differential source counts for a given flux density bin are then given by,

$$\frac{dN}{dS}\Big|_{S=S_c} = n(S_c) = \frac{N_c}{A\Delta S}, \quad (23)$$

where N_c is the number of sources in the flux density bin, A is the sky area to which the catalogue corresponds and ΔS is the bin width. Errors are estimated for the source counts by assuming Poisson statistics. We only consider bins with $N_c \geq 9$ so as to maintain a SNR ≥ 3 for each bin.

The differential source counts for C-BASS North in total intensity, applying a 20% Galactic plane mask, are plotted in Fig. 12, alongside the differential source counts for the GB6 catalogue. We can see that at low flux densities the C-BASS source counts are significantly lower. This is to be expected from the increasing catalogue incompleteness at these lower flux densities. From the differential source counts, we can again see the catalogue completeness level from the point at which the source count turn-off ends and we have good agreement between the C-BASS and GB6 counts, i.e., over flux densities $\sim 1 \text{ Jy} - 10 \text{ Jy}$. It is worth noting here that the errors obtained from assuming Poisson statistics are likely to be somewhat optimistic. These do not account for false positives in the source catalogues, or errors arising from incorrect binning due to uncertain flux density estimates. These effects become significant at lower flux densities, where the proportion of false positives in the catalogue is greater, and our photometry methods become less reliable.

We fit the usual power-law model to the differential source counts, given by,

$$\frac{dN}{dS} = n(S) = \Lambda \left(\frac{S}{S_0} \right)^\gamma, \quad (24)$$

where Λ is the count amplitude, $S_0 = 3 \text{ Jy}$ is the reference flux density and γ is the spectral index for the source counts. For C-BASS sources we perform the fit to data points above the turn-off in the source counts ($S_\nu > 750 \text{ Jy}$), where the C-BASS catalogue is largely complete. For GB6, we fit to data points over the range $S_\nu > 0.07 \text{ Jy}$, so as to avoid the need to apply correction factors to faint GB6 source counts. We assume a Gaussian likelihood, and assign the following weakly informative priors to Λ and γ ,

$$\Lambda \sim \mathcal{N}(\mu = 5, \sigma = 5), \quad (25)$$

$$\gamma \sim \mathcal{N}(\mu = -2.5, \sigma = 2.0). \quad (26)$$

In addition to the Gaussian prior, we also multiply the spectral index prior by the Jeffreys independence-rule prior,

given by,

$$p_J(\gamma) \propto \sqrt{\sum_i \left(\frac{1}{\sigma_i} \left(\frac{S_i}{S_0} \right)^\gamma \log \frac{S_i}{S_0} \right)^2}, \quad (27)$$

where σ_i is the error on the differential source count at flux density S_i ([Jeffreys 1961](#); [Eriksen et al. 2008](#)). To account for additional errors in the source counts arising from flux density uncertainties and incorrect binning of sources, we marginalize over an additional percentage error, f_{extra} , so that the total error on the source count in the i^{th} bin is given by,

$$\sigma_i = \sqrt{\sigma_{\text{Poisson}}^2 + (f_{\text{extra}} n(S_i))^2}, \quad (28)$$

where σ_{Poisson} is the Poisson error on the source count. We assign an exponential prior to the additional percentage error, $f_{\text{extra}} \sim \text{Exp}(\lambda = 20)$, corresponding to a characteristic value of 5%. We again explore our parameter space using the NUTS algorithm.

The results from these power-law fits are summarized in Table 5. When we do not apply any Galactic plane mask to the C-BASS catalogue, we fit a noticeably shallower spectral index than for the GB6 catalogue. This is driven by the excess in bright source counts in the C-BASS catalogue. This is caused by the spurious flagging of bright, blob-like emission in the Galactic plane, and the over-estimation of source flux densities in the presence of such emission, as discussed in Section 4.2. On applying a 20% Galactic plane mask the 95% HPD intervals for C-BASS and GB6 overlap as expected. This can be seen in Fig. 12, where we plot 100 posterior samples from the C-BASS and GB6 models. When we apply a 20% Galactic mask the posterior samples for the C-BASS and GB6 models overlap significantly.

5 CONCLUSIONS

We have produced a total intensity catalogue of point sources at 4.76 GHz, covering declinations $\delta \geq 10^\circ$. The catalogue was produced by filtering the whole sky using the SMHW2 filter, and contains 1729 sources. The C-BASS source catalogue has been characterized through comparisons with the pre-existing GB6 and PMN catalogues over their common declination ranges. Through these direct comparisons we estimate the C-BASS catalogue to have a 90% completeness level of approximately 630 mJy, when applying a 20% Galactic plane mask, with a corresponding reliability of 95%. The catalogue is available on request to the corresponding author, and will be made publicly available with the C-BASS northern sky data release.

These comparisons with the GB6 and PMN catalogues also enabled a number of checks to be performed on the

Table 5. Fitted power-law parameters for the differential source counts. We quote the mean parameter values and the 95% HPD intervals. Results are given for cases where we apply 0% and 20% Galactic plane masks.

Catalogue	$\langle\Lambda\rangle$	95% HPD [Λ]	$\langle\gamma\rangle$	95% HPD [γ]
C-BASS:				
0% Galactic mask	5.17	{4.35, 5.91}	-1.65	{-1.76, -1.54}
20% Galactic mask	2.86	{2.33, 3.37}	-2.37	{-2.56, -2.19}
GB6:				
0% Galactic mask	2.97	{2.60, 3.31}	-2.43	{-2.49, -2.37}
20% Galactic mask	2.45	{2.02, 2.86}	-2.48	{-2.57, -2.41}

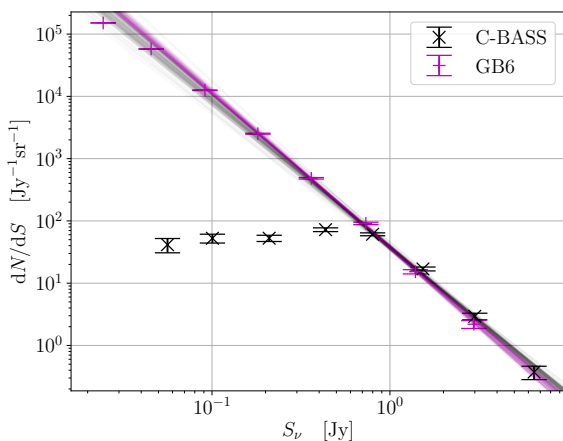


Figure 12. Differential source counts calculated using the C-BASS northern sky total intensity catalogue, plotted alongside the differential source counts for the GB6 catalogue. Source counts were calculated applying a 20% Galactic plane mask. We also plot the fitted model source counts corresponding to 100 posterior samples for the C-BASS and GB6 models. At low flux densities we note the expected lower levels in the C-BASS counts. This arises due to the fact that sources were identified in the C-BASS map that was deconvolved and smoothed to a 1° Gaussian, leading to confusion issues for faint sources, along with fainter sources being more heavily obscured by diffuse emission and noise. Good agreement between GB6 and C-BASS differential source counts is found over intermediate flux densities (~ 1 Jy – 10 Jy).

C-BASS data. We find a modal absolute positional offset of approximately 3.5 arcmin when applying a 20% Galactic plane mask. The low-level of additional scatter in positional offsets, compared to the positional uncertainty found during the algorithm validation, acts to confirm the accuracy of the C-BASS pointing. We compare the flux densities of C-BASS sources with matched sources in the GB6 and PMN catalogues, using a Gaussian mixture model to quantify the agreement between the flux density scales. Applying a 20% Galactic plane mask, we find a mean flux density ratio of $\langle\mu_{in}\rangle = 0.97$ comparing to GB6, and $\langle\mu_{in}\rangle = 1.01$ comparing to PMN. In both cases the 95% HPD intervals overlap with 1. Considering $\sim 5\%$ uncertainties in the GB6 and PMN flux density scales, we conclude that the C-BASS and GB6/PMN flux density scales are consistent.

As an additional check on the statistical properties of the bright source population in the C-BASS catalogue, we

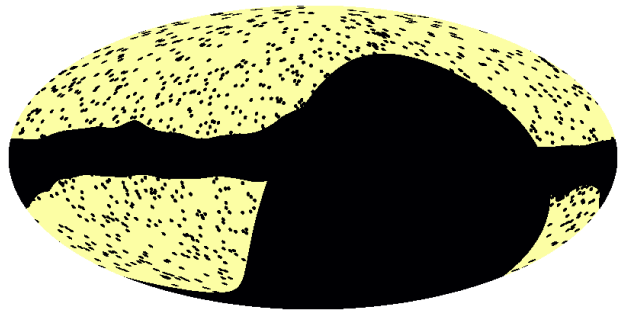


Figure 13. An example point source mask derived from the C-BASS total intensity northern sky catalogue, shown here in Galactic coordinates with masked pixels in black. In this example we mask all sources with flux densities greater than 630 mJy i.e., above the 90% completeness level obtained when applying the 20% Galactic plane mask. We mask all pixels within 1° of a source, and further mask all pixels within 2° of sources with flux densities greater than 100 Jy. In addition to masking around sources, we have masked all pixels within the 20% Galactic plane mask and all pixels corresponding to declinations $\delta < -10^\circ$, where the coverage of the C-BASS catalogue ends.

calculate the differential source counts for C-BASS sources. Applying a 20% Galactic plane mask, the C-BASS source counts show excellent agreement with the GB6 source counts over the flux density range ~ 1 –10 Jy. At lower flux densities, we see the expected turn-off in the C-BASS source counts as the C-BASS catalogue becomes more incomplete.

For the purposes of C-BASS analysis, the primary data product from this work is a total intensity point source mask, a key element of component separation analyses involving C-BASS data. In Fig. 13 we show an example point source mask derived from the C-BASS catalogue, combined with the 20% Galactic plane mask and a declination mask for $\delta < -10^\circ$. Here we mask all sources with flux densities greater than 630 mJy. We mask all pixels within 1° of a source, and further mask all pixels within 2° of sources brighter than 100 Jy. Considering only declinations, $\delta \geq -10^\circ$, this leaves 71% of the sky un-masked. In future work this will be extended to include a catalogue of polarized sources. The mask produced from this will be key for the analysis of C-BASS polarization data.

ACKNOWLEDGEMENTS

The C-BASS project is a collaboration between Oxford and Manchester Universities in the UK, the California Institute of Technology in the U.S.A., Rhodes University, UKZN and the South African Radio Observatory in South Africa, and the King Abdulaziz City for Science and Technology (KACST) in Saudi Arabia. It has been supported by the NSF awards AST-0607857, AST-1010024, AST-1212217, and AST-1616227, and NASA award NNX15AF06G, the University of Oxford, the Royal Society, STFC, and the other participating institutions. This research was also supported by the South African Radio Astronomy Observatory, which is a facility of the National Research Foundation, an agency of the Department of Science and Technology. CD and SH acknowledge support from an STFC Consolidated Grant (ST/P000649/1). CD acknowledges support from an ERC Starting (Consolidator) Grant (no. 307209). MWP acknowledges funding from a FAPESP Young Investigator fellowship, grant 2015/19936-1. We make use of the PYTHON MATPLOTLIB, NUMPY, SCIPY, HEALPY, ASTROPY, OPENCV, PYMC3 and THEANO packages (Hunter 2007; Oliphant 2006; Jones et al. 2001; Górski et al. 2005; Zonca et al. 2019; Astropy Collaboration et al. 2013, 2018; Kaehler & Bradski 2016; Salvatier et al. 2016; Al-Rfou et al. 2016).

REFERENCES

- AMI Consortium et al., 2011, *MNRAS*, **415**, 2708
 Al-Rfou R., et al., 2016, arXiv e-prints, abs/1605.02688
 Ali-Haïmoud Y., Hirata C. M., Dickinson C., 2009, *MNRAS*, **395**, 1055
 Antoine J.-P., Vanderghyest P., 1999, *Applied and Computational Harmonic Analysis*, **7**, 262
 Argüeso F., Sanz J. L., Herranz D., López-Caniego M., González-Nuevo J., 2009, *MNRAS*, **395**, 649
 Astropy Collaboration et al., 2013, *A&A*, **558**, A33
 Astropy Collaboration et al., 2018, *AJ*, **156**, 123
 Bennett C. L., et al., 2013, *The Astrophysical Journal Supplement Series*, **208**, 20
 Brandt W. N., Lawrence C. R., Readhead A. C. S., Pakianathan J. N., Fiola T. M., 1994, *ApJ*, **424**, 1
 Carvalho P., Rocha G., Hobson M. P., Lasenby A., 2012, *MNRAS*, **427**, 1384
 Cayón L., Sanz J. L., Martínez-González E., Banday A. J., Argüeso F., Gallegos J. E., Górski K. M., Hinshaw G., 2001, *MNRAS*, **326**, 1243
 Challinor A., Chon G., Colombi S., Hivon E., Prunet S., Szapudi I., 2011, PolSpice: Spatially Inhomogeneous Correlation Estimator for Temperature and Polarisation, Astrophysics Source Code Library (ascl:1109.005)
 Chapin E. L., et al., 2011, *MNRAS*, **411**, 505
 Condon J. J., 1974, *ApJ*, **188**, 279
 Condon J. J., 1984, *ApJ*, **287**, 461
 Condon J. J., Cotton W. D., Greisen E. W., Yin Q. F., Perley R. A., Taylor G. B., Broderick J. J., 1998, *AJ*, **115**, 1693
 Curto A., Martínez-González E., Barreiro R. B., 2011, *MNRAS*, **412**, 1038
 Curto A., Tucci M., González-Nuevo J., Toffolatti L., Martínez-González E., Argüeso F., Lapi A., López-Caniego M., 2013, *MNRAS*, **432**, 728
 Dickinson C., et al., 2019, *MNRAS*, **485**, 2844
 Draine B. T., 2011, Physics of the Interstellar and Intergalactic Medium
 Eriksen H. K., Jewell J. B., Dickinson C., Banday A. J., Górski K. M., Lawrence C. R., 2008, *ApJ*, **676**, 10
 Génova-Santos R., et al., 2015, *MNRAS*, **452**, 4169
 González-Nuevo J., Argüeso F., López-Caniego M., Toffolatti L., Sanz J. L., Vielva P., Herranz D., 2006, *MNRAS*, **369**, 1603
 Górski K. M., Hivon E., Banday A. J., Wandelt B. D., Hansen F. K., Reinecke M., Bartelmann M., 2005, *ApJ*, **622**, 759
 Gregory P. C., Scott W. K., Douglas K., Condon J. J., 1996, *The Astrophysical Journal Supplement Series*, **103**, 427
 Gregory P. C., Scott W. K., Poller B., 1998, in Zensus J. A., Taylor G. B., Wrobel J. M., eds, *Astronomical Society of the Pacific Conference Series Vol. 144, IAU Colloq. 164: Radio Emission from Galactic and Extragalactic Compact Sources*. p. 283
 Gregory P. C., Capak P., Gasson D., Scott W. K., 2001, in Schilizzi R. T., ed., *IAU Symposium Vol. 205, Galaxies and their Constituents at the Highest Angular Resolutions*. p. 98
 Griffith M. R., Wright A. E., 1993, *AJ*, **105**, 1666
 Griffith M. R., Wright A. E., Burke B. F., Ekers R. D., 1994, *The Astrophysical Journal Supplement Series*, **90**, 179
 Griffith M. R., Wright A. E., Burke B. F., Ekers R. D., 1995, *The Astrophysical Journal Supplement Series*, **97**, 347
 Healey S. E., Romani R. W., Taylor G. B., Sadler E. M., Ricci R., Murphy T., Ulvestad J. S., Winn J. N., 2007, *ApJS*, **171**, 61
 Healey S. E., Fuhrmann L., Taylor G. B., Romani R. W., Readhead A. C. S., 2009, *AJ*, **138**, 1032
 Herranz D., López-Caniego M., Sanz J. L., González-Nuevo J., 2009, *MNRAS*, **394**, 510
 Hoffman M. D., Gelman A., 2014, *Journal of Machine Learning Research*, **15**, 1593
 Hovatta T., Nieppola E., Tornikoski M., Valtaoja E., Aller M. F., Aller H. D., 2008, *A&A*, **485**, 51
 Hunter J. D., 2007, *Computing in Science & Engineering*, **9**, 90
 Jeffreys H., 1961, *Theory of Probability*, third edn. Oxford, Oxford, England
 Jones E., Oliphant T., Peterson P., et al., 2001, SciPy: Open source scientific tools for Python, <http://www.scipy.org/>
 Jones M. E., et al., 2018, *MNRAS*, **480**, 3224
 Kaehler A., Bradski G., 2016, *Learning OpenCV 3: Computer Vision in C++ with the OpenCV Library*. O'Reilly Media, <https://books.google.co.uk/books?id=SKy3DQAAQBAJ>
 Kovalev Y. Y., Nizhelsky N. A., Kovalev Y. A., Berlin A. B., Zhekanis G. V., Mingaliev M. G., Bogdantsov A. V., 1999, *A&AS*, **139**, 545
 Kuehr H., Pauliny-Toth I. I. K., Witzel A., Schmidt J., 1981, *AJ*, **86**, 854
 López-Caniego M., Herranz D., González-Nuevo J., Sanz J. L., Barreiro R. B., Vielva P., Argüeso F., Toffolatti L., 2006, *MNRAS*, **370**, 2047
 Mann R. G., et al., 1997, *MNRAS*, **289**, 482
 Martínez-González E., Gallegos J. E., Argüeso F., Cayón L., Sanz J. L., 2002, *MNRAS*, **336**, 22
 Massardi M., Bonaldi A., Negrello M., Ricciardi S., Raccanelli A., de Zotti G., 2010, *MNRAS*, **404**, 532
 Mesa D., Baccigalupi C., De Zotti G., Gregorini L., Mack K. H., Vigotti M., Klein U., 2002, *A&A*, **396**, 463
 Meyers B. W., et al., 2017, *Publications of the Astronomical Society of Australia*, **34**, e013
 Mingaliev M. G., Stolyarov V. A., Davies R. D., Melhuish S. J., Bursov N. A., Zhekanis G. V., 2001, *A&A*, **370**, 78
 Mingaliev M. G., Sotnikova Y. V., Bursov N. N., Kardashev N. S., Larionov M. G., 2007, *Astronomy Reports*, **51**, 343
 Næss S. K., Louis T., 2013, *Journal of Cosmology and Astro-Particle Physics*, **2013**, 001
 Nagai H., et al., 2012, *MNRAS*, **423**, L122
 Oliphant T., 2006, NumPy: A guide to NumPy, USA: Trelgol Publishing, <http://www.numpy.org/>

- Pauliny-Toth I. I. K., Witzel A., Preuss E., Kühr H., Kellermann K. I., Fomalont E. B., Davis M. M., 1978, *AJ*, **83**, 451
- Planck Collaboration et al., 2014, *A&A*, **571**, A28
- Planck Collaboration et al., 2016a, *A&A*, **594**, A6
- Planck Collaboration et al., 2016b, *A&A*, **594**, A8
- Planck Collaboration et al., 2016c, *A&A*, **594**, A9
- Planck Collaboration et al., 2016d, *A&A*, **594**, A10
- Planck Collaboration et al., 2016e, *A&A*, **594**, A26
- Pooley G. G., Ryle M., 1968, *MNRAS*, **139**, 515
- Puglisi G., et al., 2018, *ApJ*, **858**, 85
- Remazeilles M., Dickinson C., Banday A. J., Bigot-Sazy M. A., Ghosh T., 2015, *MNRAS*, **451**, 4311
- Remazeilles M., et al., 2018, *Journal of Cosmology and Astroparticle Physics*, **2018**, 023
- Richter G. A., 1975, *Astronomische Nachrichten*, **296**, 65
- Riseley C. J., et al., 2016, *MNRAS*, **462**, 917
- Rutledge R. E., Bildsten L., Brown E. F., Pavlov G. G., Zavlin V. E., 2001, *ApJ*, **551**, 921
- Salvatier J., Wiecki T. V., Fonnesbeck C., 2016, PyMC3: Python probabilistic programming framework, Astrophysics Source Code Library (ascl:1610.016)
- Sutherland W., Saunders W., 1992, *MNRAS*, **259**, 413
- Taylor A. C., Grainge K., Jones M. E., Pooley G. G., Saunders R. D. E., Waldram E. M., 2001, *MNRAS*, **327**, L1
- Tegmark M., de Oliveira-Costa A., 1998, *ApJ*, **500**, L83
- Thorne B., Dunkley J., Alonso D., Naess S., 2017, *MNRAS*, **469**, 2821
- Ulrich M.-H., Maraschi L., Urry C. M., 1997, *ARA&A*, **35**, 445
- Vierva P., Martínez-González E., Gallegos J. E., Toffolatti L., Sanz J. L., 2003, *MNRAS*, **344**, 89
- Waldram E. M., Pooley G. G., Grainge K. J. B., Jones M. E., Saunders R. D. E., Scott P. F., Taylor A. C., 2003, *MNRAS*, **342**, 915
- Waldram E. M., Bolton R. C., Pooley G. G., Riley J. M., 2007, *MNRAS*, **379**, 1442
- Wang L., et al., 2014, *MNRAS*, **444**, 2870
- Weiland J. L., et al., 2011, *ApJS*, **192**, 19
- Wright A. E., Griffith M. R., Burke B. F., Ekers R. D., 1994, *The Astrophysical Journal Supplement Series*, **91**, 111
- Wright A. E., Griffith M. R., Hunt A. J., Troup E., Burke B. F., Ekers R. D., 1996a, *The Astrophysical Journal Supplement Series*, **103**, 145
- Wright A. E., Griffith M. R., Burke B. F., Ekers R. D., 1996b, *VizieR Online Data Catalog*, **8038**
- Zonca A., Singer L., Lenz D., Reinecke M., Rosset C., Hivon E., Gorski K., 2019, *Journal of Open Source Software*, **4**, 1298
- de Zotti G., Ricci R., Mesa D., Silva L., Mazzotta P., Toffolatti L., González-Nuevo J., 2005, *A&A*, **431**, 893
- de Zotti G., Massardi M., Negrello M., Wall J., 2010, *A&ARv*, **18**, 1

This paper has been typeset from a $\text{\TeX}/\text{\LaTeX}$ file prepared by the author.